High-resolution bathymetry reveals contrasting landslide activity shaping the walls of the Mid-Atlantic Ridge axial valley

Mathilde Cannat
Equipe de Géosciences Marines, CNRS-UMR7154, Institut de Physique du Globe Paris, PRES Sorbonne, Paris Cité, France

Anne Mangeney
Equipe de Sismologie, CNRS-UMR7154, Institut de Physique du Globe Paris, Université Paris–Diderot, PRES Sorbonne, Paris Cité, France

Hélène Ondréas, Yves Fouquet, and Alain Normand
Géosciences Marines–Géochimie Métallogénie, Ifremer, Brest, France

[1] Axial valleys are found along most slow-spreading mid-ocean ridges and are one of the most prominent topographic features on Earth. In this paper, we present the first deep-tow swath bathymetry for the axial valley walls of the Mid-Atlantic Ridge. These data allow us to analyze axial valley wall morphology with a very high resolution (0.5 to 1 m compared to $\geq$ 50 m for shipboard multibeam bathymetry), revealing the role played by landslides. Slow-spreading ridge axial valleys also commonly expose mantle-derived serpentinized peridotites in the footwalls of large offset normal faults (detachments). In our map of the Ashadze area (lat. 13°N), ultramafic outcrops have an average slope of 18° and behave as sliding deformable rock masses, with little fragmentation. By contrast, the basaltic seafloor in the Krasnov area (lat. 16°38′N) has an average slope of 32° and the erosion of the steep basaltic rock faces leads to extensive fragmentation, forming debris with morphologies consistent with noncohesive granular flow. Comparison with laboratory experiments suggests that the repose angle for this basaltic debris is $> 25°$. We discuss the interplay between the normal faults that bound the axial valley and the observed mass wasting processes. We propose that, along axial valley walls where serpentinized peridotites are exposed by detachment faults, mass wasting results in average slopes $\leq 20°$, even in places where the emergence angle of the detachment is larger.

1. Introduction

[2] Axial valleys characterize slow-spreading mid-ocean ridges [*Macdonald*, 1982] and are present, with relief commonly in excess of 1000 m [e.g. *Small*, 1998], along the ~34,000 km of present-day ridges that have a spreading rate less than 5 cm/yr [*Bird*, 2003]. This makes them one of the most prominent topographic features on Earth. Axial valleys form due to slip on normal faults as a response to plate separation [*Tapponnier and Francheteau*, 1978; *Shaw and Lin*, 1996] and are seismically active areas [*Huang et al.*, 1986; *Smith et al.*, 2003]. High relief and active seismicity are favorable conditions for landslides and submersible dives have accordingly reported the widespread occurrence of talus deposits along axial valley walls [*Karson and Dick*, 1983; *Zonenshain et al.*, 1989; *Mével et al.*, 1991; *Cannat et al.*, 1997] and in DSDP and ODP holes drilled off-axis the Mid-Atlantic Ridge [*Lagabrielle and Cannat*, 1990]. Yet up to now, very few studies have addressed the role of landslides in shaping the walls of the axial valley, owing to the lack of adequately high-resolution topographic or seafloor imagery data.

[3] Shipboard bathymetry at water depths > 2000 m typically has a horizontal resolution of 50 to 100 m. With this resolution, it is only possible to map the largest, plurikilometer-sized head scars and talus lobes [*Tucholke*, 1992]. Deep tow and ROV sidescan sonar data have a better horizontal resolution [about 10 m] but have seldom been acquired outside the confines of the axial valley floor, where they provide valuable images of the volcanic constructions [e.g., *Smith et al.*, 1997]. *Tucholke et al.* [1997] described kilometer-scaled slope failures and slumps in deep tow sidescan sonar data acquired off-axis of the Mid-Atlantic Ridge (MAR). *Searle et al.* [1998] and *Grácia et al.* [2000] documented kilometer-sized cuspate head scars and debris lobes using sidescan sonar data in the MAR axial valley wall at lat. 29°N and 36°N, but their data could not resolve the finer-scale structure of these landslides. High-resolution ROV bathymetry of the north wall of the Atlantis Transform Fault next to the Lost City hydrothermal vents, also documented kilometer-scaled landslide head walls in outcrops of serpentinized peridotites [*Karson et al.*, 2006].

[4] In this paper, we use the first ROV multibeam bathymetry data acquired on a mid-ocean ridge axial valley wall. These data were acquired in 2007 during the SERPENTINE cruise of RV Pourquoi Pas? with a RESON SeaBat 7125 multi-beam echo sounder mounted on ROV Victor 6000 [*Simeoni et al.*, 2007]. The ROV was flying at a velocity of 0.3 m/s, 50 m above seafloor. With a track spacing of 120 m and 2 emissions per second, the nominal accuracy of our data is 10 cm and their nominal horizontal resolution is ~2.5 m across-track. Processing was achieved using the CARAIBES® software (IFREMER), resulting in bathymetric grids with a spacing of 0.5 (Krasnov region) and 1 m (Ashadze region). The resolution of these grids allows us to analyze the topography of the walls of the MAR axial valley with unprecedented detail. We use these data to study the fine-scale structure of submarine landslides and their role in shaping the axial valley walls. We also compare our mid-ocean ridge observations to laboratory simulations of aerial and submarine granular flows.

[5] The relief of mid-ocean ridges axial valleys is commonly used to derive tectonic characteristics of the ridge region, such as fault offset [e.g., *Escartín et al.*, 1999] and the angle of emergence of the faults at the seafloor, which reflects the amount of flexural rotation associated with faulting and is controlled by fault and footwall rheology [*Lavier et al.*, 1999; *Smith et al.*, 2008; *Cannat et al.*, 2009]. Mass wasting effects on the tectonic scarps formed at mid-ocean ridges have been discussed previously [e.g., *Escartín et al.*, 1999; *Mitchell et al.*, 2000], but our study provides unique high-resolution maps of axial landslides as constraints for this discussion.

[6] Axial valley bounding faults commonly expose deeply derived rocks such as serpentinized peridotites and gabbros [*Karson et al.*, 1987; *Cannat*, 1993]. *Mitchell et al.* [2000] performed a statistical study of seafloor slopes along submersible dive tracks. They found a tendency for basalts and gabbros to form steeper slopes than serpentinites. However, having no access to high-resolution sonar or bathymetry data, *Mitchell et al.* [2000] could not discriminate between the two possible factors which they proposed to explain this statistical tendency: a lower equilibrium slope for serpentinite outcrops, or a lower dip of faults that bound serpentinite outcrops. Our high-resolution bathymetric data concern two regions (Figure 1) of the Mid-Atlantic Ridge axial valley with contrasting outcropping lithologies [*Cherkashov et al.*, 2008]: basalts in the vicinity of the extinct Krasnov hydrothermal vent site (lat. 16°38′N) and serpentinized peridotites in the vicinity of the Ashadze hydrothermal vent site (lat. 13°N). We are therefore in a position to better document the links between lithology and the morphology of axial valley slopes.

1.1. Morphology of Axial Valley Wall Outcrops of Serpentinized Peridotite (lat. 13°N)

[7] The MAR western axial valley wall at lat. 13°N exposes serpentinized peridotites, less common

gabbros and rare basalts [*Cherkashov et al.*, 2008; *Picazo et al.*, 2012; *Ondréas et al.*, 2012]. It rises about 2500 m above the axial valley floor (Figure 1b and c), and its summit is a flat and corrugated surface, interpreted as an exhumed large offset normal fault (also called detachment) surface [*Smith et al.*, 2006]. The axial valley below this surface slopes down in two main steps (Figure 1c), each with an average slope around 18°. Shipboard bathymetry [*Smith et al.*, 2006] has sufficient resolution to image two horseshoe-shaped head scars, about 3 km in diameter, at the top of the lower step (A and B; Figure 1b) and a series of lobes in the axial valley bottom. The high-resolution bathymetry coverage extends downslope from the junction of the two horseshoe-shaped head scars (Figure 1b). It includes the Ashadze 1 hydrothermal vent site at a depth of 4090 m [*Cherkashov et al.*, 2008; *Ondreas et al.*, 2012] and reveals complex finer-scale features, illustrated in

Figure 2 and which we will now describe, using the shaded bathymetry (Figure 2a), the corresponding slope map (Figure 2b), and a 3D view of the bathymetry (Figure 3).

[8] Going downslope from the northwestern corner of the microbathymetric map (Figure 2a) at 3400 m, we first follow a narrow southeast-trending ridge, which forms the junction between the two large head scars visible on the shipboard bathymetry (A and B in Figure 1b). Terrains to the south of this narrow ridge belong to landslide B and display a series of northeast-trending scarps (Figure 2), up to 50 m high and spaced by 2 to 20 m which we interpret as secondary slope failures within the large B landslide. Terrains to the north of the narrow southeast-trending ridge belong to landslide A and dip about 30° to the northeast. At a depth of about 3500 m, we get to a prominent cuspate head scar with a diameter of about 700 m and a height of about 200 m (scar 1 in Figures 2 and 3). The slid
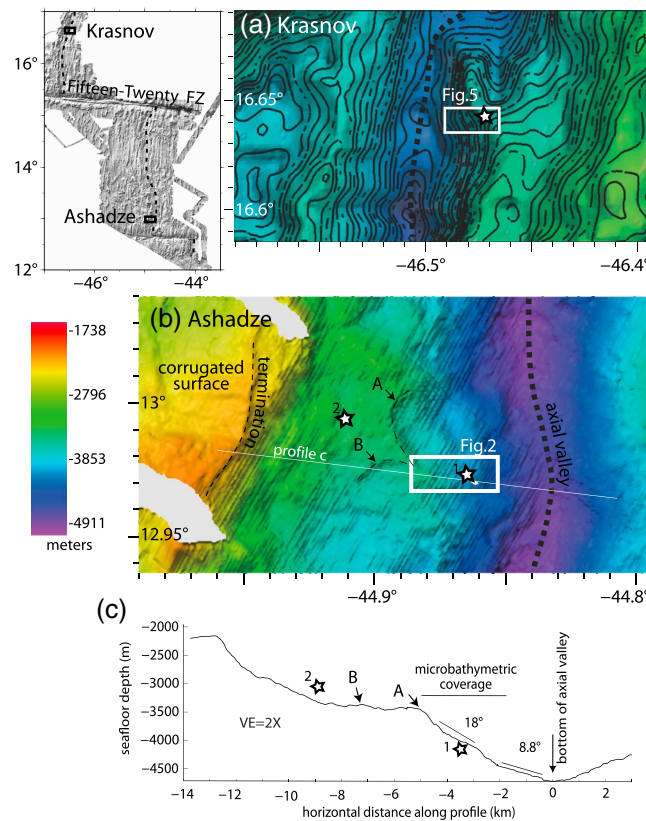

Figure 1. Location and regional context of the Krasnov and Ashadze high-resolution bathymetric maps of the Mid-Atlantic Ridge axial valley wall (white rectangles in a and b). Stars show location of hydrothermal sites Krasnov (a) and Ashadze 1 and 2 (b). (a) Krasnov area. Shipboard multibeam data acquired during the RIDELENTE cruise of RV Jean Charcot in 1988. (b) Ashadze area. Multibeam data from *Smith et al.* [2006] show from west to east an old corrugated surface, then the axial valley wall with two hemicircular landslide scars (A and B), then the axial valley floor with lobe-shaped features that may be landslide deposits. (c) Across-axis profile of the axial valley wall (map location in b).

material below scar 1 is cut first by two linked horseshoe scars that accommodate an additional 100 m drop (scar 2 in Figures 2 and 3), then by a series of 1- to 5-m-high cuspate ENE-facing scarps which we interpret as multiple gravitational failure surfaces (domain labeled as fissured slide material in Figures 2 and 3).

[9] At a depth of 4000 m, this fissured slide domain ends in a 75-m-wide shallow north-south graben (Figures 2 and 3). Below this graben, seafloor morphology changes to smoother and gentler slopes, and we infer that it is a more coherent rock mass than the pervasively fissured material above. At a depth of about 4030 m, there is a 25-m-high east-facing scarp (scar 3). Below this scarp, slopes remain moderate (<10°; Figure 2), and the terrain displays short NE and NNE-trending steps, which we propose are formed due to slope failure along preexisting fractures in the relatively coherent sliding rock mass. Scar 3 ends to the north against an ESE-trending lineament that aligns upslope with the junction of the two cuspate segments of scar 2 (Figure 2). Downslope this lineament can be followed to about 4250 m and aligns with the limits of debris lobes visible at depths greater than 4300 m. We

propose that this lineament represents the northern lateral limit of a sliding rock mass originating at scar 2 and forming a subset of the main scar 1 landslide (Figure 2). En echelon fissures visible next to this lineament just above scar 3 (Figures 2a and 3) suggest left lateral displacement, consistent with this interpretation. To the north of this lineament, there is another scarp, which we named scar 3', although it is not clearly connected to scar 3. To the south, scar 3 is cut by yet another horseshoe-shaped landslide (scar 4), with a diameter of about 500 m, which also cuts across the southern lateral ramp of scar 1 (Figures 2 and 3). Just below scar 4, there is a 100-m-wide, 60-m-deep excavation which could have formed due to large rock falls from the steep lateral ramp of scar 1 above. Decameter-sized debris lobes are barely visible below this excavation, on slopes of 10° to 16°, but this touches the limit of the map resolution (Figure 2).

[10] Below 4150 m, slopes become progressively steeper over the full width of the mapped area: 16°, then > 30°, with erosion features in the form of excavations and possible gullies (Figure 3b). Three observations lead us to infer a recent tectonic, rather than gravitational origin for these steeper slopes: they have no head scar, they have a convex upward profile
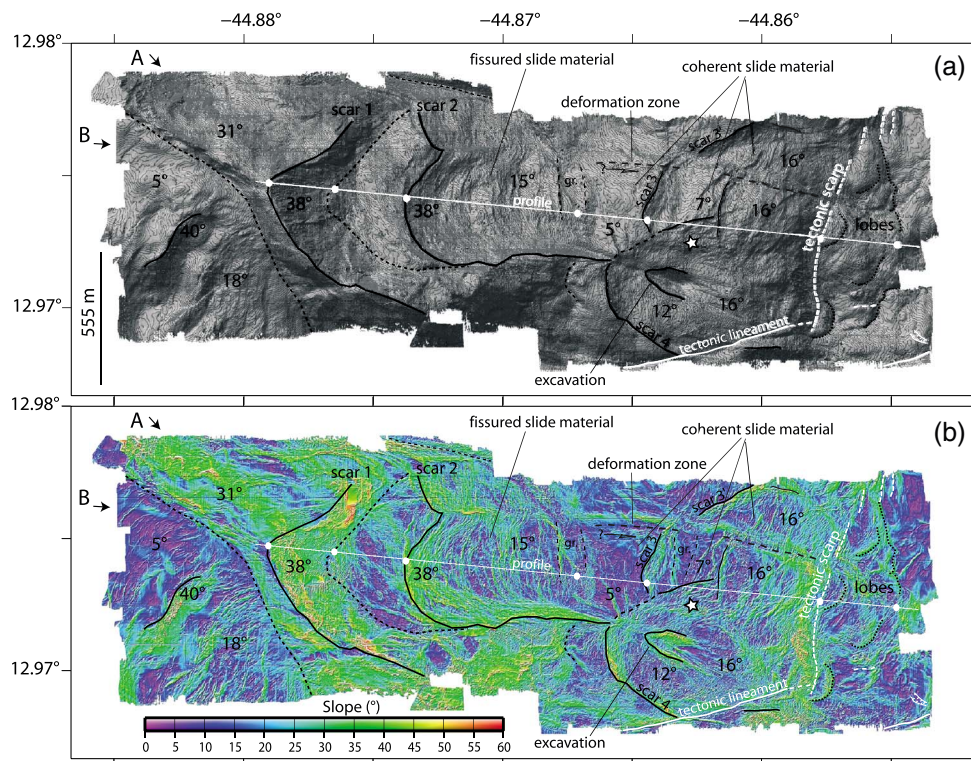

Figure 2. Shaded high-resolution bathymetry (a) with added contours spaced by 2 m in fine grey lines and slope map (b) for the area of the axial valley wall mapped next to the Ashadze 1 vent site (location in Figure 1b). A structural interpretation is overlain: structures outlined in black are inferred to result from slope failure processes; those outlined in white are interpreted as tectonic (see text). Profile is shown in Figure 4.
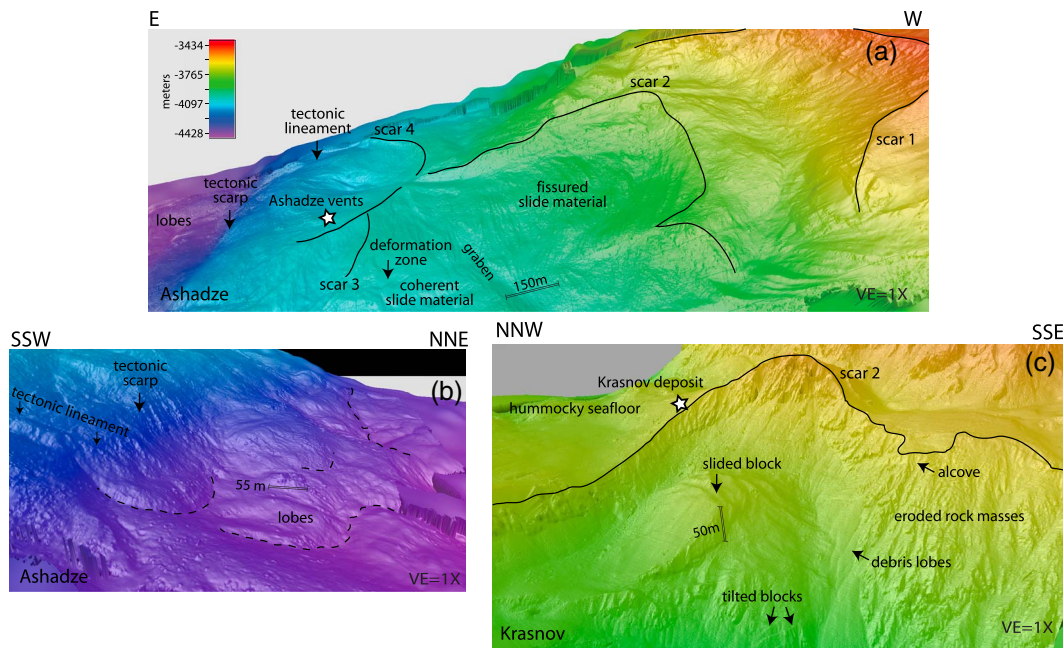
Figure 3. 3D views (with common color scale) of the high-resolution bathymetry at the (a and b) Ashadze and (c) Krasnov locations. (a) 3D view of the Ashadze 1 venting area, looking down from the north. The main slope failure structures are shown as in Figure 2. Note the clear step in bathymetry corresponding with the NNE-trending tectonic scarp, inferred to be associated with recent normal faulting. (b) 3D view from the SE to the lower slopes of the Ashadze map. Note erosion scars on inferred tectonic scarp, and lobe-shaped features below it. Also note NE-trending lineament inferred to be dominantly strike–slip recent fault cutting into erosion alcoves and lobes. (c) 3D view from the SW to the upper slopes of the Krasnov map. The sulphide deposit (star) has been partially eroded and forms part of the slid block below scar 2. Also note ubiquitous smaller-scale erosion features (alcoves, gullies, and lobes).

while the landslide scars produce dominantly concave upward slopes (Figure 4a), and there is a clear slope break between these steep slopes and the more gently sloping debris lobes below (Figures 2 and 3).

[11] Another feature of the map that is probably tectonic in origin is an ENE-trending lineament in the southeast corner of the map (Figures 2 and 3b). It is marked either by a 2- to 5-m-wide depression, or by a meter-high north-facing scarp that cuts through the excavations of the steep lower slope domain. Given its linear trend and surficial expression, we propose that it is dominantly a recent strike–slip fault. At the southeastern corner of the map, a similar lineament is visible, with the same orientation, and 40 m north of this feature, there is a 20-m-wide and 3-m-deep fissure in the debris deposit (Figure 2). Near the northeastern corner of the map, the terrain appears very smooth, but bears NNE-trending lineaments that are parallel to the main tectonic scarp. We infer that these could be splays of the same fault system, cutting into the deposits.

[12] Our analysis of the microbathymetry at Ashadze, therefore, shows that, with the exception of a few structures in the lower slopes for which we infer a tectonic origin, seafloor morphology is dominated by structures related to slope failure. These include three main head scars (scars 1, 2, and 4; Figures 2 and 3a), a pervasively fissured upper slide domain and then a more coherent rock mass down to a series of debris lobes that appear to have been deformed by more recent tectonic lineaments. The distance between the master head scar (scar 1) and these lobes is 2.6 km, and the cumulated vertical displacement along the slide is of the order of 300 m (height of the 2 main scarps). We also see en echelon fissures and slope-parallel lineaments which we infer result from differential movements within the sliding rock mass. Slopes are typically less than 18° in the slide material (Figure 4a and b).

1.2. Morphology of Axial Valley Wall Outcrops of Basalt (lat. 16°38′N)

[13] The MAR western axial valley wall at lat. 16°38′N has only been sampled in the vicinity of the extinct Krasnov vent site, where it exposes basalt and massive sulphides [*Cherkashov et al.*, 2008]. Available shipboard bathymetry in this region has a very low resolution, showing only the broader-scale features such as the two shelves
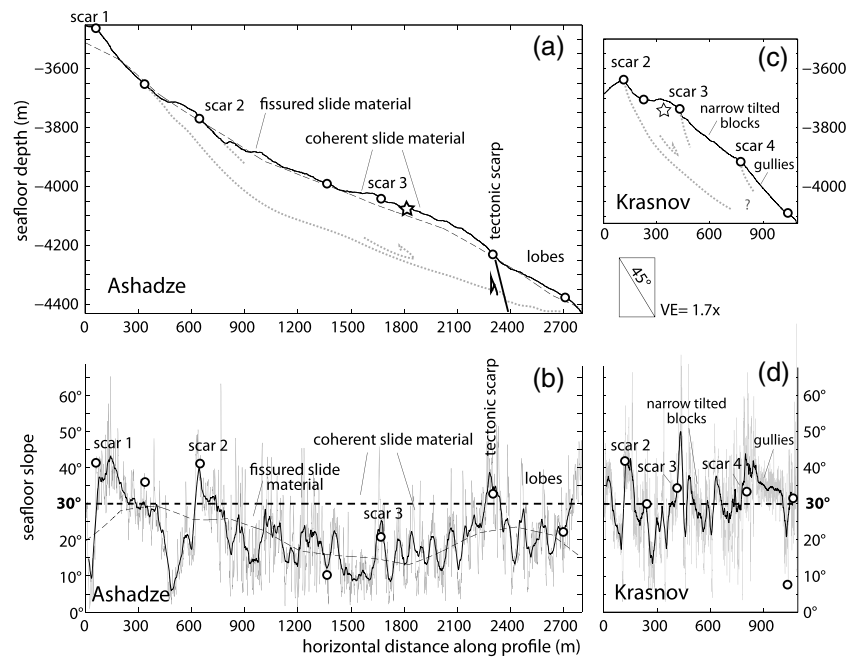
Figure 4. Depth and slope profiles across the high-resolution bathymetry maps at Ashadze (a and b; location of profile in Figure 2), and Krasnov (c and d; location of profile in Figure 5). Along profile distances, depths and slopes are shown at the same scale for the Ashadze and Krasnov areas. Raw slope profiles are shown as thin grey lines in b and d; thicker black lines are 40 m slope moving averages. Possible landslide geometries are sketched in dotted lines in a (Ashadze) and c (Krasnov). Dashed lines in a and b correspond to shipboard, lower resolution yet excellent bathymetry (*Smith et al.*, 2006). Note the dominantly low slope values in the ultramafic seafloor of the Ashadze area, compared to dominantly higher slopes in the basalt seafloor of the Krasnov area.

that form the eastern axial valley wall (Figure 1a) and the NS trending ridge that sticks out of the lower shelf north of the Krasnov fossil vent site. The high-resolution bathymetry (Figures 3c and 5) extends downslope from this lower axial valley wall shelf at ~3600 m to the axial valley floor at ~4400 m. It includes the Krasnov extinct hydrothermal vent site at a depth of ~3700 m.

[14] From east to west, we first see rounded hills 50 to 200 m across, which we interpret as sedimented hummocky [*Smith et al.*, 1997] volcanic seafloor (Figure 5a and b). A NNE-trending scar (scar 1) delineates a steep west-facing scarp with a down drop of up to 100 m. This first scarp may be tectonic in origin but is clearly degraded, with semicircular excavations (alcoves) up to 50 m in diameter. The Krasnov sulphide deposit and the hummocky sedimented seafloor around it form a pervasively fissured bench that slopes gently to the NE (Figure 5). The fissures have a NW trend, perpendicular to the slope direction and may thus have a gravitational origin.

[15] The Krasnov bench is limited to the south and west by a curvilinear scarp that has a cuspate central region next to the sulphide deposit (scar 2; Figure 3c) and extends out of the map to the NW and to the south (Figure 5). This scarp is about 40 m high in the center of the cuspate region and higher away from it (about 200 m at the southern edge of the map and 350 m at the northern edge). It is steep (35° on average) and shows alcoves and erosion channels that feed aprons of debris lobes with slopes of 32° to 34° (Figures 3c and 5).

[16] Below the central cuspate region of scar 2, we see the gently sloping top of a sliding rock mass, which is cut by a second head scar at 3755 m (scar 3; Figure 5), accommodating 10 m of further down drop, then by a third head scar (scar 4) at ~3920 m and again by a fourth head scar (scar 5) at ~4130 m, which is barely visible at the southern limit of the map. This succession of landslides is shown in cross-section in Figure 4c and d. It is specific to the slopes beneath the central cuspate region of scar 2. In the other areas, the upper slopes below scar 2 do not show coherent sliding blocks, but a combination of four seafloor morphologies (Figure 5): rock masses forming steep (40° or more) cliffs with erosion channels; debris lobes that surround these eroded rock masses and typically
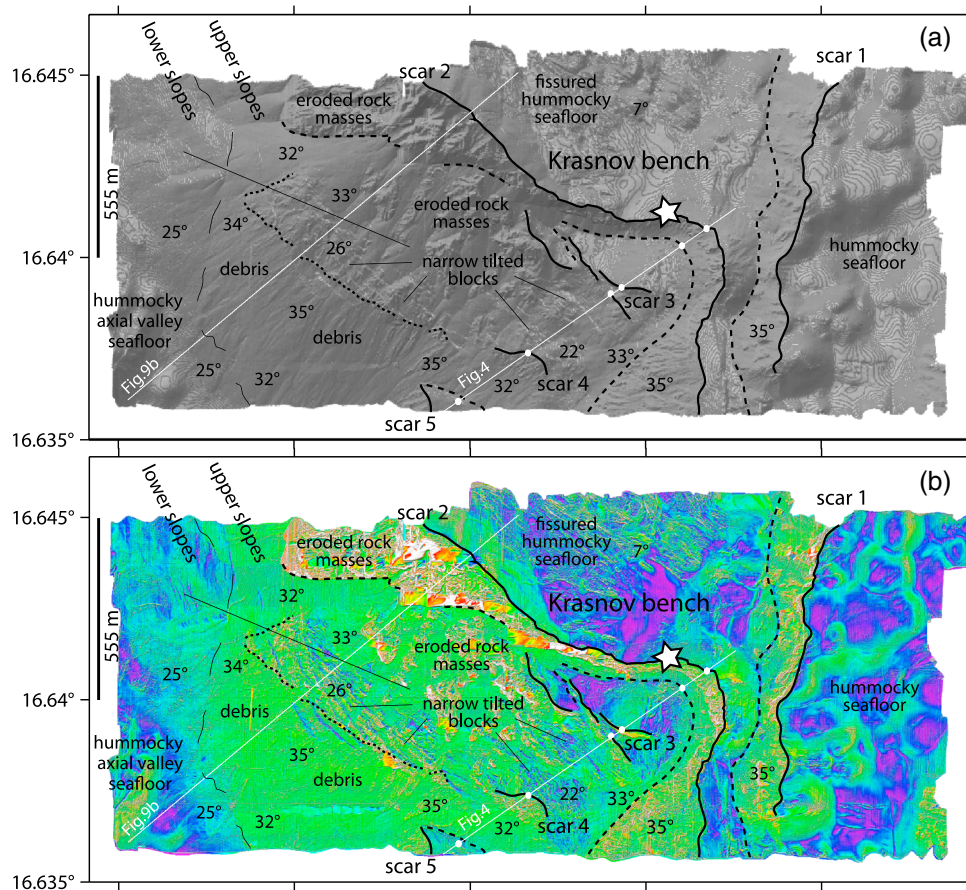
Figure 5. Shaded high-resolution bathymetry (a- with added contours spaced by 2 m in fine grey lines) and slope map (b) for the area of the axial valley wall mapped next to the Krasnov sulphide deposit (star; location in Figure 1b). Color scale for slopes as in Figure 2b. A structural sketch is overlain (see text).

have slopes of 32° to 34° (Figure 6b, c, and d); domains of gentler average slopes (22° to 26°) that are made of narrow tilted blocks; and steep slopes (34°-35°) with gullies and finger-shaped debris deposits (Figures 5 and 6e and f). Below these upper slopes, the axial valley wall curves into the valley floor via a domain of lower slopes (25°) and more rounded debris lobes (Figures 5 and 6a).

[17] The tilted blocks are less than 10 m wide and 20 to 50 m apart (Figure 7a), with eastward (antithetic) slopes up to 18°. They mostly affect the eroded rock masses in the upper slopes of the mapped domain (Figure 5), but some can be seen to cut into the gullies and into the deposits of the upper and lower slopes (for example in Figures 3c and 7a). Some individual tilted blocks can be followed up to 300 m laterally. Their NNW dominant trend is perpendicular to average slopes in the map area but commonly oblique to the local slopes (for example, see Figure 7a). We infer that these hectometer-scale slope failure structures are active and provide a sustained influx of debris to

the domains of gullies and finger-shaped debris lobes below (Figure 5).

[18] Our analysis of the microbathymetry at Krasnov shows that, with the possible exception of the uppermost N-trending scarp above Krasnov bench (scar 1), which may be a normal fault relief, seafloor morphology is dominated by structures related to slope failure, with a main head scar (scar 2) at ~3700 m, degraded rock masses that have average slopes > 40° and domains of debris flows and tilted blocks that have slopes of 24° to 35°. The average slope of the axial valley wall below scar 2 and down to the axial valley floor at ~4400 m is ~32° (Figure 4d).

2. Discussion

2.1. Contrasted Morphology of Ultramafic and Basaltic Axial Valley Walls

[19] The contrast between the axial valley wall morphology at Ashadze (Figure 2) and Krasnov
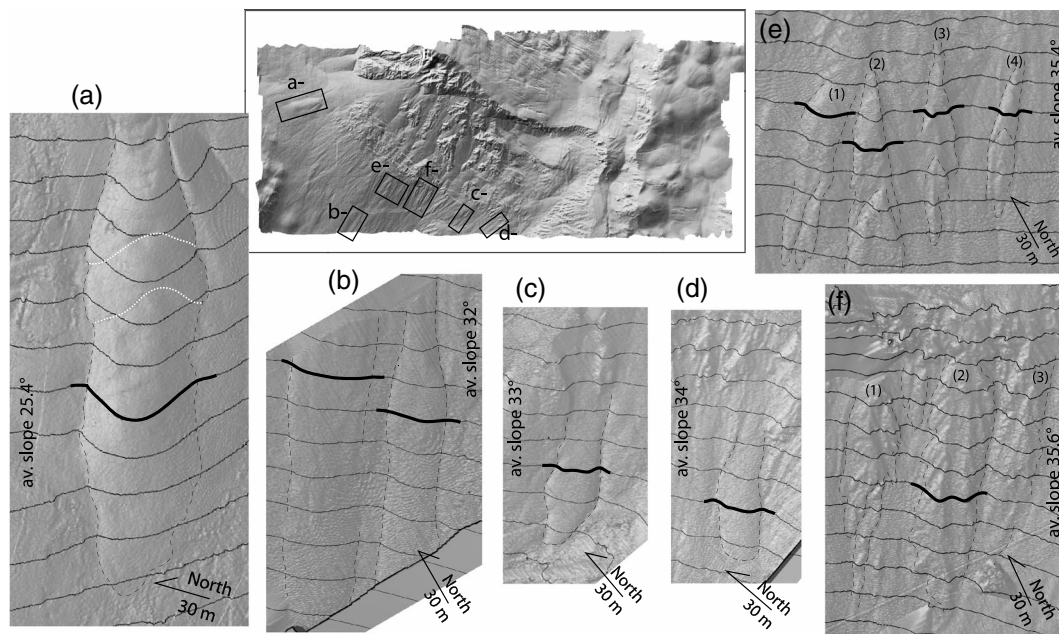
Figure 6. Morphology of rockslide deposits in the Krasnov area (basaltic seafloor). Detailed maps are all at the same scale (North arrow is 30 m long), and the profiles used to compute the deposits thickness values plotted in Figure 8a are located with bold lines. (a) A broad and round-shaped deposit in an area of moderate slopes (~25° on average next to the deposit). This deposit shows 2 successive curved and decimeter-high steps (white dotted lines; see also Figure 1 in Appendix); (b) two long finger-shaped deposits near edge of map, originating in the steeper slopes above (Figure 5); (c and d) short finger-shaped deposits (average slopes 33–34°) originating in curvilinear excavations or alcoves visible above deposits; (e) four enigmatic triangular-faced structures on slopes ~35°. These lens-shaped structures are ~15 m wide and up to 2.5 m high and rest on very planar and regular slopes; (f) three complex deposits on slopes ~35°. The one in the center (2) shows a well-developed central channel which we propose could be syndepositional. It also shows complex fishbone-like lateral gullies, which we interpret as erosion features.

(Figure 5) concerns two principal characteristics: 1) the average slope of the axial valley wall, which is much less in the ultramafic (Ashadze, 18°) than in the basaltic (Krasnov, 32°) environment and 2) the occurrence and morphology of decameter-sized debris flows. These are widespread with a range of shapes (Figure 6) at all levels of the basaltic slopes (Figures 3c and 5). By contrast, in the ultramafic slopes, we observed rounded debris lobes only at the very bottom of the mapped area (Figures 2 and 3b). The morphology of these lobes is complex and suggests that they have been deformed by recent axial tectonics.

[20] The difference in slopes between our basaltic and ultramafic case study areas is consistent with the statistical difference identified by *Mitchell et al.* [2000] between submersible dive tracks in ultramafic and basaltic mid-ocean ridge outcrops. However, the statistical best slope values determined by *Mitchell et al.* [2000]: 32° for ultramafic seafloor and 42° for basaltic seafloor, are significantly larger than the average slopes measured in our study. This discrepancy is probably due to the

fact that submersible surveys are commonly targeted to the steepest slopes in any given region, where chances to sight massive outcrops are better.

[21] *Mitchell et al.* [2000] discussed two possible causes for this contrast in slopes: faults that expose serpentinized peridotites could have a lower dip than faults in basalts, or serpentinized material could have a lower equilibrium slope. Axial valley bounding faults have indeed been observed to emerge at greater angles in basaltic than in ultramafic environments. In basaltic environments, axial valley normal faults typically have dips $\geq 45°$ [*Thatcher and Hill*, 1995; *Tucholke et al.*, 1997]. By contrast, in ultramafic environments, emergence angles $\leq 15°$ and as low as 4° have been documented for actively emerging detachment faults at the Mid-Atlantic Ridge north of Ashadze [*Smith et al.*, 2006; *MacLeod et al.*, 2009]. The resulting very low-angle exhumed fault surfaces bear corrugations and are not significantly eroded. By contrast, the ultramafic outcrops at Ashadze dip, as shown here, 18° on average and are extensively affected by landslides. This indicates that the emergence angle of the fault exhuming these
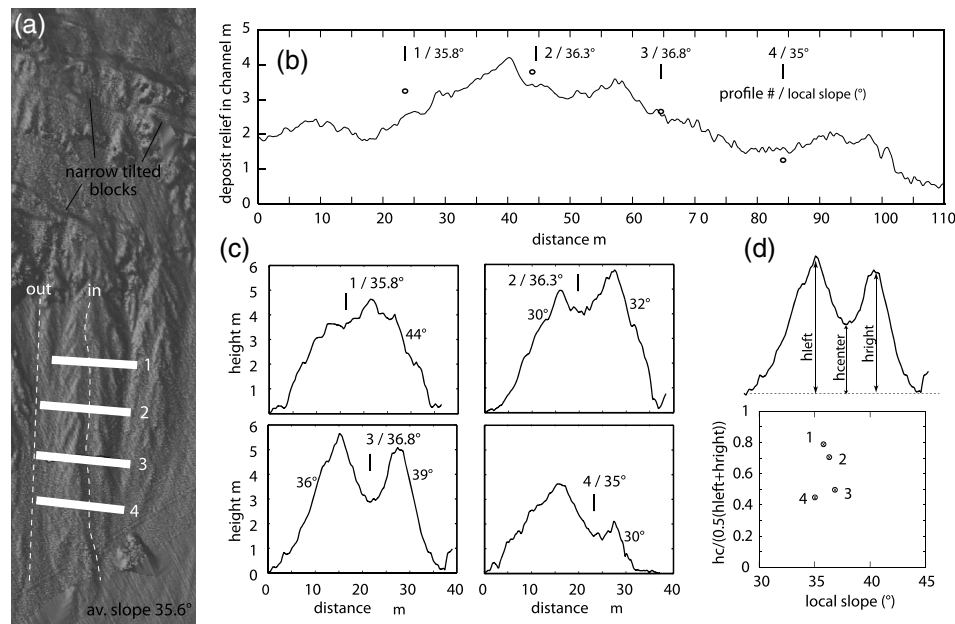
Figure 7. Krasnov area. Morphology of finger-shaped deposit with fishbone-like structures and central channel (deposit 2 in Figure 6f). (a) Shaded high-resolution bathymetric map with location of a down-channel profile (dashed "in" line). Deposit relief along this profile is shown in b after subtraction of baseline topography (dotted "out" line in a). Dots in b show the deposit relief measured on each across-channel profile. Four across-channel profiles are shown in c with indication of the levee slopes. Profile numbers and local slopes (measured for each across-channel profile for a 15-m-long portion of the down-channel profile) are indicated, as well as local across-channel slopes for the levee ramps (see text). (d) Sketch showing our definition of deposit's thickness $h_{central}$ (h_c). The diagram shows the ratio of h_c over the mean of the height of the left and right levees (h_{levee}) as a function of the local slope.

ultramafic rocks was greater than the rocks equilibrium angle. Higher angles of fault emergence have been proposed during the initiation stages of axial detachments before significant flexural rollback has occurred [*Lavier et al.*, 1999]. The amount of rollback associated with mature detachments may also vary depending on the strength of the footwall and of the fault region [e.g., *Cannat et al.*, 2009].

[22] Our observations also suggest that ultramafic rocks and basalts do not behave similarly with respect to gravitational mass-wasting. The morphology of the ultramafic seafloor mapped in the Ashadze region (Figures 2 and 3) suggests that the rock masses below successive head scars behave as cohesive sliding blocks, with internal deformation resulting in fractures and fissures and indicating extension within the sliding mass, but little fragmentation and consequently few debris deposits. We also observe features such as the EW strike slip deformation zone above scar 3 (Figure 2), which could accommodate differential motions within the sliding blocks. This recalls observations made in the underwater Storegga Slide [*Micallef et al.*, 2007]. The morphologies observed at Ashadze also show similarities with those of clay-bearing creeping landslides observed at onland locations [e.g., *Rutter and Green*, 2011]. These observations are not consistent with granular flow of noncohesive mass-wasted material being a dominant mechanism. Instead, they suggest a component of viscoplastic deformation within the sliding rock mass. It is also worth noting that head scars in the Ashadze map appear to have formed successively downward and preferentially across the lateral ramps of previous landslides: scar 1 cutting across the ramp between the larger hemicircular scars A and B (Figures 1b and 2), then scar 4 cutting across the south ramp of scar 1 (Figure 2).

[23] By contrast, over half of the surface of axial valley wall mapped in the Krasnov region appears to be covered with debris flows, including rounded or finger-shaped pluridecameter-sized deposits (Figures 3c, 5, and 6). This shows that erosion of the steep basaltic rock faces leads to extensive fragmentation. Although we do not have dive observations for the debris flows at Krasnov, the mapped morphologies (steep rock faces, narrow tilted blocks and extensive talus) are typical of dive observations reported for basaltic seafloor elsewhere along the Mid-Atlantic Ridge [*Karson and*

Dick, 1983; *Zonenshain et al.*, 1989; *Mével et al.*, 1991; *Cannat et al.*, 1997]. Basalt talus along these dive tracks is seen to be made of angular blocks, most commonly 0.3 to 0.7 m in size (Figure 8b).

2.2. Mass-wasting in Basaltic Material: Insight from Granular Flow Physics

2.2.1. Morphology of the Deposits and Qualitative Comparison with Granular Flow Experiments

[24] The high-resolution map of the Krasnov area offers an opportunity to further analyze the morphology of the deposits and discuss their formation with regard to granular flow physics and analogue experiments. Figure 6 shows examples of the deposits identified in the Krasnov area. It shows that slopes around 25° near the base of the axial valley wall occasionally display broad and round-shaped deposits (Figure 6a). Deposits

observed on steeper slopes (32–34°) are smaller and more finger-shaped (Figure 6b, c, and d). Finally, the steeper slopes (~35°), just below the massive rock faces of the upper axial valley wall, display more complex morphologies (Figure 6e and f). These morphologies comprise triangular-faced structures (Figure 6e), deposits with fishbone-like lateral gullies and, in one case, a well-developed central channel (Figure 6f and 7).

[25] The broad and rounded deposit in Figure 6a is 55 m wide and 7.5 m high and displays small curvilinear steps a few decimeters in height. It looks very similar to deposits formed in laboratory experiments by noncohesive granular flow over inclined planes at small fluxes and/or slopes *Félix and Thomas*, 2004. These experimental deposits are also rounded and exhibit small steps on their surface (photograph in Figure 8c). Finger-shaped deposits up to 30 m wide and 2.5 m high are
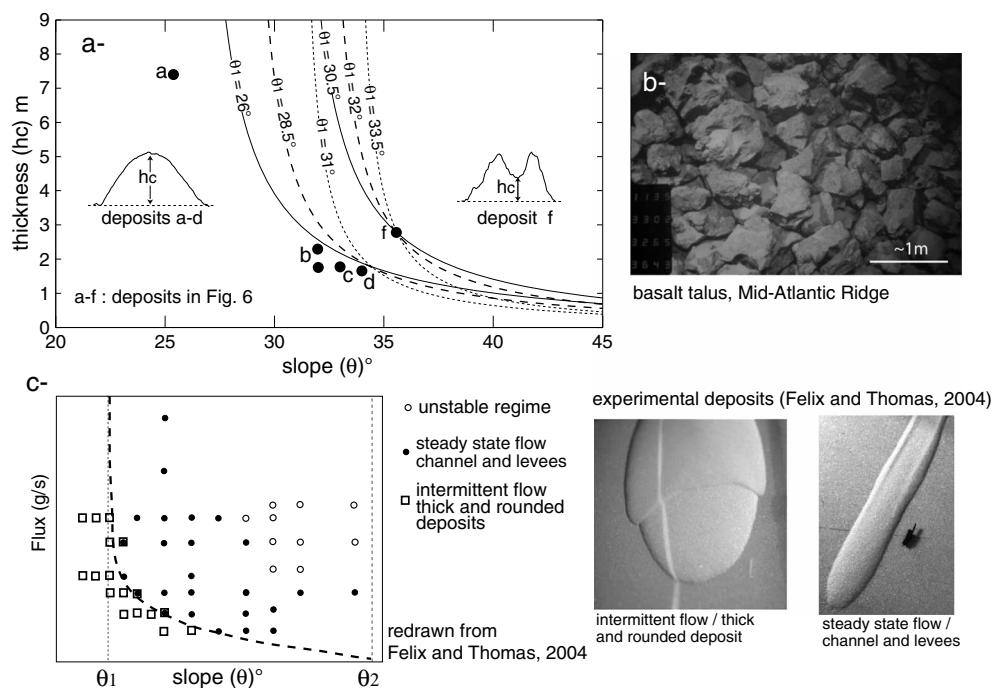

Figure 8. Morphologic characteristics of deposits in the Krasnov area and comparison with results of granular flow experiments. (a) Thickness versus slope (θ) characteristics for the deposits shown in Figure 6. h_c is thickness of deposit (in channel for channel-levee deposit of Figure 6f). Dashed lines are calculated with Equation (1) for a particle size of 0.5 m, $a = 0.3$ (thin lines), 0.5 (dashed), or 0.7 (dotted) and a range of θ_1 values. In laboratory experiments, θ_1 is found to be close to the repose angle of the granular material involved [*Félix and Thomas*, 2004]. Values of $\theta_1 \geq 26°$ are needed in order for the rounded deposits (Figure 6a, b, c, and d) to plot under the curve, as predicted for granular flow deposits (see text). The levee-channel deposit of Figure 6f, if its central channel did form during deposition, should plot approximately on the curve (see text). This condition is met for $33.5° \geq \theta_1 \geq 30.5°$. (b) Typical talus of basalt blocks photographed from Nautile submersible in the MAR axial valley wall at lat. 15°30′N, showing dominant size of blocks around 0.5 m [Faranaut cruise; *Cannat et al.*, 1997]. (c) Results of laboratory granular flow experiments by *Félix and Thomas*, [2004]. Flux versus slope diagram is redrawn after their Figure 11. Photographs of their experimental deposits are shown at similar scales (pencil cap).

observed in domains of steeper slopes (32°–34°). Some are short and originate in nearby excavations (Figure 6c and d), while others are > 150-m-long (Figure 6b).

[26] The triangular-faced structures in Figure 6e (35° slope) are lens-shaped, ~15 m wide and up to 2.5 m high. The corridors between these structures may be erosion channels feeding the finger-shaped deposits down below (Figure 6). These corridors, however, have a very regular and planar slope, suggesting that they could be floored by talus aprons. The triangular-faced structures occasionally terminate into narrower lobes, suggesting that they are indeed deposits. They show triangular-shaped steps that could be due to successive destabilizations of an initial deposit. Alternatively, these structures could result from surface instabilities that have been shown to develop during deposition at high slopes and/or fluxes in subaerial and submarine environments [Figure 1 in *Forterre and Pouliquen*, 2003; Figure 4 in *Cassar et al.*, 2005].

[27] The three complex deposits in Figure 6f also rest on slopes ~35°. The one on the left (deposit 1 in Figure 6f) displays an asymmetrical pattern of erosion gullies and a sinuous channel that could be a post-deposition erosion feature. However, it also resembles the sinuous channels and complex morphologies observed for some natural debris and pyroclastic flows inland [*Calder et al.*, 2000; *Lube et al.*, 2007; *Mangold et al.*, 2010; *Jessop et al.*, 2012]. These natural complexities deserve a more systematic study that would require in-situ observations that are not presently available. Deposit 2 in Figure 6f has an almost constant width (25–35 m) and shows fishbone-like lateral gullies and a well-developed central channel with lateral levees (~2–6 m thick). The gullies that form these fishbone-like structures are similar to erosion gullies commonly seen on head scars (for example in Figure 6d) and could be due to meter-scaled rockslides. Figure 7 details the morphology of deposit 2. It is 2 to 4 m thick in the central channel and displays a drop in relief about 1 m down profile (Figure 7b), which may be the deposit front, although this cannot be confirmed because there are artefacts in the high-resolution bathymetry in this part of the map (corresponding to the pale grey wedge-shaped area in Figure 5a). There are two possible explanations for the origin of this channel: 1) an erosive channel that would have been generated at the top surface of a preexisting lobe or 2) a levee-channel deposit similar to the deposits formed in laboratory experiments of noncohesive granular flow over inclined planes at high fluxes and/or slopes *Félix and Thomas*, 2004]. Note that such experimental deposits are also of near constant

width (photograph in Figure 8c). With the available data, we cannot exclude erosion as the origin. However, we favor the second interpretation (levee-channel deposit) because the channel is so central (Figure 7a): erosive flows essentially follow the steeper slope direction rather than the higher elevations. Thus, despite the great complexity of the geomorphological structures in the Krasnov region, similarities can be pointed out with deposits observed at the laboratory scale for noncohesive granular material in subaerial environments. In the following paragraphs, we review significant results obtained in granular flow experiments and numerical modeling and use these results to gain insight into the possible properties of the rockslides in the Krasnov region. In doing so, we must keep in mind that our interpretation of the observed deposits is not definitive and that additional data, particularly in-situ observations, will be needed for confirmation of this interpretation, particularly regarding the possible levee-channel deposit in Figure 6f.

2.2.2. Granular Flow Characteristics and Properties

[28] In recent years, a wide range of laboratory experiments on granular flows and their numerical modeling have helped to better understand and quantify the origin of natural geomorphological structures, even though these experiments did not reproduce the full complexity of natural flows, such as the real topography, nature, and shape of the material involved, solid/fluid interactions, erosion processes, etc. [*Pouliquen and Vallance*, 1999; *Félix and Thomas*, 2004; *Cassar et al.*, 2005; *Mangeney et al.*, 2007; *Pelanti et al.*, 2008; *Fernandez-Nieto et al.*, 2008; *Mangeney et al.*, 2010]. Indeed, application of scaling laws or identification of flow regimes observed experimentally can provide first estimates of the frictional and dynamic properties of natural flows [*Lucas and Mangeney*, 2007; *Jessop et al.*, 2012].

[29] Experiments on unconfined dry granular matter flowing down an inclined plane show that several flow regimes exist depending on the input flux and the inclination of the plane [*Félix and Thomas*, 2004; Figure 8c]. Each flow regime corresponds to a particular morphology of the associated deposit. For small flux and/or slopes, intermittent granular flows are observed. At higher flux and/or slopes, the flow reaches a steady state and the deposit exhibits a levee/channel morphology as observed for aerial debris flows or pyroclastic flows [e.g., *Lube et al.*, 2007; *Mangold et al.*, 2010; *Jessop et al.*, 2012]. The variation of the thickness of the central channel (between the levees) as a function of the slope angle

$h_c(\theta)$ is shown to be very similar to the variation with slope angle of the maximum thickness of the deposit of steady uniform flows over inclined planes, usually called $h_{stop}(\theta)$ [*Pouliquen*, 1999a; Figure 9 in *Félix and Thomas*, 2004; *Mangeney et al.*, 2007]. Indeed, the pioneering experiments of *Pouliquen* [1999a] show that steady uniform granular flows are observed in a given range of inclination angles [θ_1, θ_2] when a constant upstream supply is imposed. When the supply is cut, a uniform deposit of thickness $h_{stop}(\theta)$ is obtained. This thickness reflects the frictional properties of the granular material and its interaction with the rough bed [*Pouliquen and Forterre*, 2002; *GDR MiDi*, 2004]. Several empirical relations have been proposed to fit the $h_{stop}(\theta)$ curve [*Pouliquen*, 1999; *Pouliquen and Forterre*, 2002; *Börzsönyi et al.*, 2008] which make it possible to fit a wide range of experiments using very different particles (material, grain size and shape) for appropriate empirical parameters. As in *Jessop et al.* [2012], we choose here the following empirical relationship for $h_c(\theta)$: (Equation 1)

$$\frac{h_c(\theta)}{d_p} = \frac{a}{tan\theta - tan\theta_1}$$

where d_p is the particle diameter, a is the dimensionless constant and θ_1 the vertical asymptote of the $h_c(\theta)$ curve, which is very close to the repose angle of the material involved [*Börzsönyi et al.*, 2008; *Mangeney et al.*, 2010, p 6]. In the experiments, the flow thickness $h > h_c$ strongly depends on the initial flux of material, while h_c seems to be almost independent of the flow [*Félix and Thomas*, 2004]. As observed for the curve representing the input flux as a function of the slope angle θ (Figure 8c), the $h_c(\theta)$ curve also separates different flow regimes. For flow thicknesses h below the curve, the deposit has a rounded shape. Under these conditions, even if the deposit is continuously supplied with granular matter coming from upslope, the flow is intermittent: successive flows start from an accumulation zone and spread down the slope covering the previous flow [*Félix and Thomas*, 2004]. When feeding stops, the provided volume may not be enough for complete coverage and a step forms (left photograph in Figure 8c). For flow thicknesses above the curve, the levee-channel morphology exists except when instabilities occur (high angle and thickness). The levee-channel morphology, with some matter remaining in the channel, occurs only between slope angles θ_1 and θ_2 [*Félix and Thomas*, 2004]. These experiments were performed in the subaerial environment. However, the experiments of *Cassar et al.* [2005] show that the $h_{stop}(\theta)$ curve is very similar for subaerial and submarine granular flows (their Figure 3). For confined flows, this curve separates similar regimes for the subaerial and submarine case. As a result, it may be expected that qualitatively similar regimes would be obtained for subaerial and submarine unconfined granular flows.

2.2.3. Quantitative Comparison and Frictional Properties Deduced for Krasnov Deposits

[30] We measured the thickness h_{center} of the central part of the lobe (Figure 8) and the mean slope θ of the topography under the deposit θ for the deposits shown in Figures 6 and 7. The ratio $h_c/h_{levee}(\theta)$ for the possible levee-channel deposit ranges between 0.4 and 1 (Figure 7d), similar to the range measured by *Jessop et al.* [2012] for pyroclastic flows and by *Félix and Thomas* [2004] for laboratory experiments. The levee slope in the direction perpendicular to the flow is observed to be a few degrees smaller than θ_1 in the laboratory experiments of *Félix and Thomas* [2004]. In the deposit shown in Figure 7, however, we measured a wide range of levee slopes (up to 44°; Figure 7c). We propose that the fishbone-shaped erosion ridges and troughs observed on the sides of this deposit (Figure 7a) induced significant changes of the local slope.

[31] We tried to make the $h_c(\theta)$ curve (Equation 1) go through the data (Figure 8a) for a range of values of the empirical constant a (0.3, 0.5, and 0.7) and with the typical grain diameter taken as $d_p = 0.5$ m (consistent with dive observations in basaltic talus at the Mid-Atlantic Ridge; Figure 8b). As explained above, the constraint is that the rounded deposits should be under the curve, while the inferred levee-channel deposit should be approximately on the curve. In Figure 8a, we show that the minimum θ_1 value that fits the first condition (rounded deposits under the curve) is 26°. If the deposit in Figure 6f is indeed a levee-channel granular flow deposit, the range of θ_1 values that fit the second condition (levee-channel deposit on the curve) is between 30.5° and 33.5°. Note that these empirical values are within the range of those obtained by *Börzsönyi et al.* [2008] and *Mangeney et al.* [2010] who found a $\in$ [0.26, 0.66] and θ_1 $\in$ [20.5°, 32.6°] for different materials from spherical glass beads to irregularly shaped salt and copper flowing on rough beds. In laboratory experiments, θ_1 is found to be close to the repose angle of the granular material involved [*Félix and Thomas*, 2004]. The above analysis therefore suggests an angle of repose of at least 26° for the natural basaltic material in the axial valley slopes at Krasnov.

2.3. Interplay Between Tectonic and Mass Wasting Processes Control the Relief of Mid-Ocean Ridge Axial Valleys

[32] Axial valley relief at slow-spreading ridges is created as a response to normal faulting that accommodates part of the plate separation. In Figure 9, we propose that rockslides (in the basaltic environment at Krasnov) and creep in a cohesive sliding rock mass (in the ultramafic environment at Ashadze) occur continuously as tectonic displacement proceeds on the axial valley wall bounding fault(s). In the basaltic environment at Krasnov, this mass-

wasting behavior is primarily controlled by small-scale structures (decameter-sized rockslides) that may initiate after only a small fault relief has been created, then proceed continuously as fault offset increases (Figure 9b). By contrast in the ultramafic environment at Ashadze, the mass-wasting behavior is controlled by a large landslide (Figure 9a) that must have formed after the fault had created a few hundred meters of relief. At a horizontal fault displacement rate of 1 cm/yr, for a critical landslide triggering relief estimated at 500 m and depending on the emergence angle of the fault, this could take between 42 kyrs (fault emergence angle = 50°) and
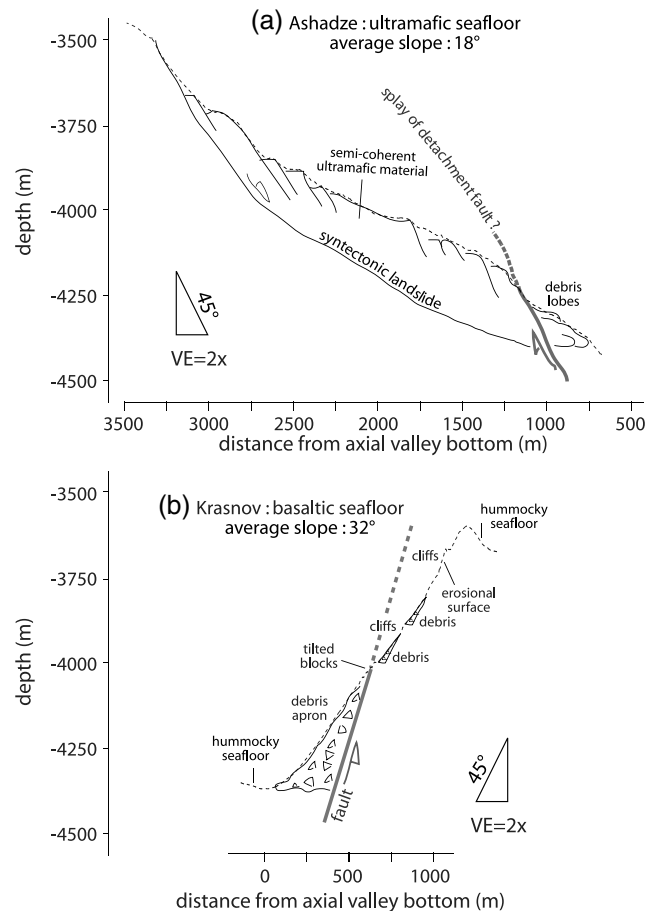

Figure 9. Sketches showing the contrasted axial valley wall morphologies associated with ultramafic or basaltic seafloor. The interplay between normal faulting and mass-wasting in both settings is also tentatively sketched. Topography is drawn (dashed line) from actual bathymetry in the Ashadze and Krasnov areas (profiles located in Figures 2 and 5) and inferred landslide or rockslide geology is sketched in thin black lines. Axial valley relief in both cases originates due to the main axial valley bounding fault. In the case of the ultramafic seafloor (a) the landslide material behaves as a deformable but semicoherent rock mass and the landslide is deformed by a fault that could represent the emergence of the detachment fault that exhumes mantle-derived material over the whole axial valley wall in this region. Alternatively, this fault (tectonic lineament shown in Figures 2 and 3a–b) may be a splay of this detachment. In the case of the basaltic seafloor, (b) the cumulated displacement along the fault is known because hummocky volcanic seafloor is offset by about 900 m from the axial valley floor to the rift shoulder (Figure 5). The angle of the fault is inferred to be ~50°, with a proposed emergence about midway upslope, at the level of the tilted blocks domain (Figure 5). The rock masses above have been significantly eroded, forming cliffs that feed the debris apron below.

107 kyrs (fault emergence angle = 25°). After this large landslide has formed, our observations in the lower part of the axial valley wall at Ashadze suggest that the rock masses were significantly modified and able to creep in a more continuous fashion, while deformation proceeded. This suggests the possibility for a bimodal mass-wasting behavior of ultramafic slopes, before and after the formation of hectometer-scale landslides. We propose that the scarp interpreted as tectonic in the lower part of the Ashadze map (Figures 2 and 3b) is the trace of a normal fault, with an emergence angle ≥30°. This fault may represent the present-day emergence of the main axial detachment fault, or of one of its splays (Figure 9a).

[33] Our observations in the Ashadze region suggest that slope failure in the ultramafic rocks that form the axial valley wall limits the overall slope to ~18° when the angle of emergence of the exhumation fault exceeds this value. Such a low equilibrium angle could be due to the combined effects of three factors: (1) the abundance of weak hydrous minerals such as serpentine and talc present in the exhumed ultramafic rocks [*Picazo et al.*, 2012]; (2) sub-surface active hydrothermal processes promoting in situ mineral alteration and high temperatures [*Ondréas et al.*, 2012]; and (3) weakness zones created by the landslide sliding surfaces and fractures (Figure 9a). At this point, we do not have constraints on which of these factors are preeminent, and we lack similar high-resolution mapping for ultramafic slopes in other regions of the Mid-Atlantic Ridge. Near-bottom bathymetry at the Atlantis Massif [30°N; *Karson et al.*, 2006] shows kilometer-sized arcuate head scarps in the ultramafic rocks that form the top of the Atlantis Transform wall, next to the Lost City hydrothermal vents. These high-resolution data do not extend to the landslides below these head scarps. However, the average slope of the Atlantis Transform wall in the less well-resolved shipboard bathymetry below is ~20°, suggesting equilibrium slopes similar to those at Ashadze.

3. Conclusions

[34] This paper is the first report on high-resolution near-bottom bathymetry data for the axial valley walls of the Mid-Atlantic Ridge. Our two mapped areas are small but they allow us to resolve seafloor structures with a far better resolution than shipboard bathymetry for two contrasted types of seafloor geology: a basaltic seafloor in the

Krasnov area (lat. 16°38′N) and an ultramafic seafloor in the Ashadze area (lat. 13°N). We expect that future microbathymetric studies of more axial valley wall locations will add diversity to the picture drawn from our observations. Our principal results are as follows:

(1) Mass-wasting structures are ubiquitous in the two mapped areas. Such structures should thus be expected to contribute significantly to the fine-scale geology of the uppermost oceanic crust accreted at axial valley-bearing mid-ocean ridges.

(2) Although head scars and sliding blocks are found in our two study areas, mass-wasting operates differently in these two areas. In the Ashadze area, the serpentinized peridotites at the outcrop behave as sliding rock masses, developing fissures but little fragmentation and consequently few debris deposits. The average slope in these sliding units is 18°, suggesting that this could be the equilibrium slope angle for the ultramafic seafloor in our study area. We infer that weak hydrous minerals associated with hydrothermal alteration could favor this dominantly viscous behavior. By contrast, basaltic seafloor in our high-resolution map of the Krasnov area has an average slope of 32° and the erosion of steep basaltic rock faces leads to extensive fragmentation, forming numerous debris flows. The morphologies of these debris flows are consistent with noncohesive granular flow with an angle of repose > 25°.

(3) Mass-wasting in our two study areas is a response to relief and slopes created by the continuing activity of axial valley bounding normal faults. In the Ashadze area, we observe tectonic scarps and lineaments that cut sliding rock masses and are themselves subjected to erosion. In the Krasnov area, erosional scars and slope failure features (decameter-sized tilted blocks) that affect preexisting deposits are consistent with tectonic slope reactivation. Based on our observations in the Ashadze area, we propose that tectonic-erosion interplays result in average slopes ≤ 20° in regions of the axial valley walls where detachment faults expose deeply derived rocks in the seafloor, even if the emergence angle of the detachment is larger.

Acknowledgments

References

Bird, P. (2003), An updated digital model of plate boundaries, *Geochem. Geophys. Geosyst.*, *4*(3), 1027.

Börzsönyi, T., T. C. Halsey, and R. E. Ecke (2008), Avalanche dynamics on a rough inclined plane, *Phys. Rev. E.*, *78*, 011306.

Calder, E. S., R. S. J. Sparks, and M. C. Gardeweg (2000), Erosion, transport and segregation of pumice and lithic clasts in pyroclastic flows inferred from ignimbrite at Lascar Volcano, Chile, *J. Volcanol. Geoth. Res.*, *104*, 201–235.

Cannat, M. (1993), Emplacement of mantle rocks in the seafloor at mid-ocean ridges, *J. Geophys. Res. Sol. Earth.*, *98*(B3).

Cannat, M., Y. Lagabrielle, H. Bougault, J. de Casey, N. Coutures, L. Dmitriev, and Y. Fouquet (1997), Ultramafic and gabbroic exposures at the Mid-Atlantic Ridge: Geological mapping in the 15 N region, *Tectonophy.*, *279*, 1–4, 193–213.

Cannat, M., D. Sauter, J. Escartín, L. Lavier, and S. Picazo (2009), Oceanic corrugated surfaces and the strength of the axial lithosphere at slow-spreading ridges, *Earth Planet. Sci. Lett.*, *288*(1), 174–183.

Cassar, C., M. Nicolas, and O. Pouliquen (2005), Submarine granular flows down inclined planes, *Phys. Fluids*, *17*, 103301.

Cherkashov, G., V. Bel'tenev, V. Ivanov, L. Lazareva, M. Samovarov, V. Shilov, T. Stepanova, G. Glasby, and V. Kuznetsov (2008), Two new hydrothermal fields at the Mid-Atlantic Ridge, *Mar. Georesour. Geotechnol.*, *26*(4), 308–316.

Escartin, J., P. Cowie, R. Searle, S. Allerton, N. Mitchell, C. MacLeod, and A. Slootweg (1999), Quantifying tectonic strain and magmatic accretion at a slow-spreading ridge segment, Mid-Atlantic Ridge, 29 N: *J. Geophys. Res.*, *104*(B5), 10,421–10,437.

Félix, G., and N. Thomas (2004), Relation between dry granular flow regimes and morphology of deposits: formation of levées in pyroclastic deposits, *Earth Planet. Sci. Lett.*, *221*(1–4), 197–213.

Fernandez-Nieto, E., F. Bouchut, D. Bresch, M. J. Castro-Diaz, and A. Mangeney (2008), A new Savage-Hutter type model for submarine avalanches and generated tsunami, *J. Comp. Phys.*, *227*(16), 7720–7754.

Forterre, Y., and O. Pouliquen (2003), Long-surface-wave instability in dense granular flows, *J. Fluid Mech.*, *486*, 21–50.

GDR Midi (2004), On dense granular flows, *E. Phys. J. E.*, *14* 367–371.

Grãcia, E., J. Charlou, J. Radford-Knoery, and L. Parson (2000), Non-transform offsets along the Mid-Atlantic Ridge south of the Azores (38 N–34 N), Ultramafic exposures and hosting of hydrothermal vents: *Earth Planet. Sci. Lett.*, *177*(1–2), 89–103.

Huang, P., S. Solomon, E. Bergman, and J. Nabelek (1986), Focal depths and mechanisms of Mid-Atlantic Ridge earthquakes from body waveform inversion, *J. Geophys. Res.*, *91*, 579–598.

Jessop, D., K. Kelfoun, P. Labazuy, A. Mangeney, O. Roche, J. L. Tillier, M. Trouillet, and G. Thibault (2012), LiDAR derived morphology of the 1993 Lascar pyroclastic flow deposits, and implication for flow dynamics and rheology, *J. Volcano. Geotherm. Res.*, 245–246, 81–97.

Karson, J., and H. Dick (1983), Tectonics of ridge-transform intersections at the Kane Fracture Zone, *Mar. Geophys. Res.*, *6*(1), 51–98.

Karson, J. A., G. Thompson, S. E. Humphris, J. M. Edmond, W. B. Bryan, J. R. Brown, A. T. Winters, R. A. Pockalny, J. F. Casey, and A. C. Campbell (1987), Along-axis variations in seafloor spreading in the MARK area: *Nature*, *328*(20), 681–685.

Karson, J. A., G. L. Früh-Green, D. S. Kelley, E. A. Williams, D. R. Yoerger, and M. Jakuba (2006), Detachment shear zone of the Atlantis Massif core complex, Mid-Atlantic Ridge, 30°N, *Geochem. Geophys. Geosyst.*, *7*(6), Q06016, doi:10.1029/2005GC001109.

Lagabrielle, Y., and M. Cannat (1990), Alpine Jurassic ophiolites resemble the modern central Atlantic basement, *Geology*, *18*(4), 319–322.

Lavier, L., Roger W. Buck, and A. Poliakov (1999), Self-consistent rolling-hinge model for the evolution of large-offset low-angle normal faults, *Geology*, *27*(12), 1127.

Lube, G., S. J. Cronin, T. Platz, A. Freundt, J. N. Procter, C. Henderson, and M. F. Sheridan (2007), Flow and deposition of pyroclastic granular flows: A type example from the 1975 Ngauruhoe eruption, New Zealand, *J. Volcanol. Geoth. Res.*, *161* (3), 165–186.

Lucas, A., and A. Mangeney (2007), Mobility and topographic effects for large Valles Marineris landslides on Mars, *Geophys. Res. Lett.*, *34*, L10201.

MacDonald, K. C. (1982), Mid-ocean ridges: Fine scale tectonic, volcanic and hydrothermal processes within the plate boundary zone, *Annu. Rev. Earth Planet. Sci.*, *10*, 155.

Macleod, C. J., R. C. Searle, B. J. Murton, J. F. Casey, C. Mallows, S. C. Unsworth, K. L. Achenbach, and M. Harris (2009), Life cycle of oceanic core complexes, *Earth Planet. Sci. Lett.*, *1–12*, doi:10.1016/j.epsl.2009.08.016.

Mangeney, A., F. Bouchut, N. Thomas, J. Vilotte, and M. Bristeau (2007), Numerical modeling of self-channeling granular flows and of their levee-channel deposits, *J. Geophys. Res.*, *112*.

Mangeney, A., O. Roche, O. Hungr, N. Mangold, G. Faccanoni, and A. Lucas (2010), Erosion and mobility in granular collapse over sloping beds, *J. Geophys. Res.*, *115*(F3), F03040.

Mangold, N., A. Mangeney, V. Migeon, V. Ansan, A. Lucas, D. Baratoux, and F. Bouchut (2010), Sinuous gullies on Mars: Frequency, distribution, and implications for flow properties, *J. Geophys. Res.*, *115*(E11), E11001, doi:10.1029/2009JE003540.

Mével, C., M. Cannat, P. Gente, E. Marion, J. Auzende, and J. Karson (1991), Emplacement of deep crustal and mantle rocks on the west median valley wall of the MARK area (MAR, 23 N), *Tectonophysics*, *190*(1), 31–53.

Micallef, A., D. G. Masson, C. Berndt, and D. A. V. Stow (2007), Morphology and mechanics of submarine spreading: A case study from the Storegga Slide, *J. Geophys. Res.*, *112*(F3), F03023, doi:10.1029/2006JF000739.

Mitchell, N., M. Tivey, and P. Gente (2000), Seafloor slopes at mid-ocean ridges from submersible observations and implications for interpreting geology from seafloor topography, *Earth Planet. Sci. Lett.*, *183*(3–4), 543–555.

Ondreas, H., M. Cannat, Y. Fouquet, and A. Normand (2012), Geological context and vents morphology of the ultramafic-hosted Ashadze hydrothermal areas (Mid-Atlantic Ridge 13°N): *Geochem. Geophys. Geosyst.*, *13*, Q0AG14, doi:10.1029/2012GC004433.

Pelanti, M., F. Bouchut, and A. Mangeney (2008), A Roe-Type Scheme for Two-Phase Shallow Granular Flows over Variable Topography, *Math. Model. Numeric. Analy.*, (ESAIM: M2AN), *42*, 851–885.

Picazo, S., M. Cannat, A. Delacour, J. Escartín, S. Rouméjon, and S. Silantyev (2012), Deformation associated with the

denudation of mantle-derived rocks at the Mid-Atlantic Ridge 13°–15°N, The role of magmatic injections and hydrothermal alteration, *Geochem. Geophys. Geosyst.*, *13*, Q04G09, doi:10.1029/2012GC004121.

Pouliquen, O. (1999a), Scaling laws in granular flows down rough inclined planes, *Phys. Fluids*, *11*, 542–548.

Pouliquen, O. (1999b), On the shape of granular fronts down rough inclined planes, *Phys. Fluids*, *11*, 1956–1958.

Pouliquen, O., and J. W. Vallance (1999), Segregation induced instabilities of granular fronts, *Chaos*, *9*, 621–630.

Pouliquen, O., and Y. Forterre (2002), Friction law for dense granular flows: application to the motion of a mass down a rough inclined plane, *J. Fluid Mech.*, *453*, 133–151.

Rutter, E. H., and S. Green (2011), Quantifying creep behaviour of clay-bearing rocks below the critical stress state for rapid failure: Mam Tor landslide, Derbyshire, England: *J. Geol. Soc.*, *168*(2), 359–372, doi:10.1144/0016-76492010-133.

Searle, R. C., P. A. Cowie, N. C. Mitchell, S. Allerton, C. J. Macleod, J. Escartín, S. M.Russell, P.A. Slootweg, and T. Tanaka (1998), Fault structure and detailed evolution of a slow spreading ridge segment: The Mid-Atlantic Ridge at 29 N, *Earth Planet. Sci. Lett.*, *154*(1), 167–183.

Shaw, W., and J. Lin (1996), Models of ocean ridge lithospheric deformation: Dependence on crustal thickness, spreading rate, and segmentation, *J. Geophys. Res.*, *101*(B8), 17977.

Simeoni, P., J. Sarrazin, P. M. Sarradin, H. Ondreas, C. Scalabrin, J. M. Sinquin, and H. Nouze (2007), Victor 6000: New high-resolution tools for deep sea research, *Oceans*, 1–6.

Small, C. (1998), Global systematics of mid-ocean ridge morphology, in *Faulting and Magmatism at Mid-Ocean Ridges*, Geophysical Monograph 106, pp. 1–25, AGU.

Smith, D., J. Cann, and J. Escartin (2006), Widespread active detachment faulting and core complex formation near 13 N on the Mid-Atlantic Ridge, *Nature*, *442*, doi:10.1038/nature04950.

Smith, D., J. Escartin, M. Cannat, M. Tolstoy, C. Fox, D. Bohnenstiehl, and S. Bazin (2003), Spatial and temporal distribution of seismicity along the northern Mid-Atlantic Ridge (15°–35° N), *J. Geophys. Res.*, *108*, 2167.

Smith, D., J. Escartín, H. Schouten, and J. Cann (2008), Fault rotation and core complex formation: Significant processes in seafloor formation at slow-spreading Mid-Ocean Ridges (Mid-Atlantic Ridge, 13°–15° N), *Geochem. Geophys. Geosyst.*, *9*(3).

Smith, D., S. Humphris, M. Tivey, and J. Cann (1997), Viewing the morphology of the Mid-Atlantic Ridge from a new perspective, *EOS Trans.*, *78*, 265–265.

Tapponnier, P., and J. Francheteau (1978), Necking of the lithosphere and the mechanics of slowly accreting plate boundaries, *J. Geophys. Res.*, *83*(B8), 3955–3970.

Thatcher, W., and D. Hill (1995), A simple model for the fault-generated morphology of slow-spreading mid-oceanic ridges, *J. Geophys. Res.*, *100*(B1), 561–570.

Tucholke, B. (1992), Massive submarine rockslide in the rift-valley wall of the Mid-Atlantic Ridge, *Geology*, *20*(2), 129.

Tucholke, B., W. Kenneth Stewart, and M. Kleinrock (1997), Long-term denudation of ocean crust in the central North Atlantic Ocean, *Geology*, *25*(2), 171.

Zonenshain, L., M. Kuzmin, A. Lisitsin, Y. A. Bogdanov, BV Baranov (1989), Tectonics of the Mid-Atlantic rift valley between the TAG and MARK areas (24°–26° N): Evidence for vertical tectonism, *Tectonophysics*, *159*(1–2), 1–23.